PNAS Nexus, 2026, **5**, pgag272
https://doi.org/10.1093/pnasnexus/pgag272
Published: 12 August 2026
Physical Sciences and Engineering

Diffusive buckling fronts in lattice-based metamaterials

Jochem G. Meijer[1]*, **Faadil H. Shaik**[1], **Victoria V. McDermott**[1], and **Heinrich M. Jaeger**[1,2]

[1]James Franck Institute, The University of Chicago, Chicago, IL 60637, USA
[2]Department of Physics, The University of Chicago, Chicago, IL 60637, USA
*To whom correspondence should be addressed: Email: jgmeijer@uchicago.edu
Edited By Bahareh Behkam

Abstract

Mechanical metamaterials can be designed to exhibit unique mechanical properties, including tunable auxetic behavior as well as multistability, which arise from the geometry and configuration of the constituent building blocks. Lattice-based metamaterials, in particular, provide lightweight platforms where local instabilities can dictate the global response, with applications in energy routing and vibration isolation. In underdamped structures, perturbations have been found to propagate as nonlinear waves, e.g. transition waves or solitons. Here we investigate the opposite limit of overdamped, highly dissipative lattice metamaterials. Focusing on 3D structures, we uncover how buckling instabilities, triggered by compression, propagate as fronts that shape the macroscopic behavior. We demonstrate in experiments on 3D-printed simple cubic lattices how global and local buckling modes can be controlled via the lattice geometry. By incorporating viscoelastic dissipation into a 3D-continuum model, we show that strain-driven buckling fronts obey coupled reaction–diffusion equations. The diffusion and reaction coefficients, determined by local geometry, material properties, and strain, select the propagation direction and enable steering of the fronts. This establishes a predictive and experimentally validated framework for the control of cascading mechanical instabilities in lattice-based metamaterials.

Keywords metamaterials, lattice structures, buckling, diffusive fronts

Significance Statement

Materials under compression will eventually break, bend, or buckle—instabilities typically considered undesirable. However, suitably architected structures can exploit instabilities for new mechanical functionality. In particular, when local buckling events are designed to propagate in a controlled manner they can transform a metamaterial's mechanical properties and in the process absorb large amounts of energy. Currently, little is known about how such propagation proceeds in 3D structures that are highly dissipative. We show with experiments and modeling that strain-driven buckling instabilities in 3D-printed, overdamped lattices form fronts that evolve according to a coupled set of reaction–diffusion equations with geometry-, material-, and strain-dependent coefficients, which enables manipulation and steering of the fronts. These findings expand the design space for programmable, dissipative mechanical metamaterials.

Introduction

A uniform, slender beam under sufficient compression will undergo a buckling instability, which causes a transition from a straight configuration to a new bent shape or state (1). Instead of such global deformation under load, appropriately chosen internal architectures in mechanical metamaterials can generate instabilities that produce local deformation and/or rotation of subunits (2). The coupling between the subunits can then result in cascading instabilities that sweep through the material and transform its behavior. One prominent example is a plate with a dense array of circular holes in a periodic square pattern (3, 4). Under small uniaxial compression all holes simply flatten and become elliptical, while the overall strain response stays elastic with a positive Poisson's ratio $\nu > 0$. But beyond a critical strain, buckling leads to alternating ellipse orientations, each rotated 90° with respect to its four neighbors. This generates material contraction transverse to the applied strain and thus auxetic behavior, i.e. $\nu < 0$ (5–13).

The dynamics of cascading buckling events have so far been investigated almost exclusively in 2D structures (6, 14–21) and

Received: December 30, 2025. **Accepted:** August 3, 2026
© The Author(s) 2026. Published by Oxford University Press on behalf of National Academy of Sciences.
This is an Open Access article distributed under the terms of the Creative Commons Attribution-NonCommercial License (https://creativecommons.org/licenses/by-nc/4.0/), which permits non-commercial re-use, distribution, and reproduction in any medium, provided the original work is properly cited. For commercial re-use, please contact reprints@oup.com for reprints and translation rights for reprints. All other permissions can be obtained through our RightsLink service via the Permissions link on the article page on our site—for further information please contact journals.permissions@oup.com.

Downloaded from academic.oup.com/pnasnexus/article/5/8/pgag272/8759452 by guest on 04 November 2026

metabeams (22). In underdamped, inertial systems it has additionally been shown that external excitations can trigger transition waves (23–27) or solitons (28–35) that propagate through elastic 1D chains or 2D sytems. These traveling perturbations can form well-characterized domain walls and can also interfere with the local architecture, allowing for the creation and tuning of bandgaps (26, 36). Further complexity is added by the introduction of dissipative, viscoelastic materials with inherent internal time-scales. This gives rise to shape-changing and snapping, controlled by the experienced strain rate (21, 37–42), leading to dissipative energy transport (43), and the emergence of 1D diffusive kinks (44). However, so far there have been no systematic studies extending these concepts to buckling in 3D lattice-based metamaterials, where such kinks generalize into strain-driven, diffusive buckling fronts.

Here, we investigate buckling in 3D simple cubic lattices, fabricated by 3D-printing and subjected to uniaxial compression. These materials are highly dissipative and the compression occurs at a fixed rate that is sufficiently slow to mitigate the role of inertia. We map out the conditions for different buckling modes and to explain the experimental observations derive a set of coupled reaction–diffusion equations. This model, which is of a type more commonly used to analyze pattern evolution in biological or chemical systems (45–48), dictates the emergence of local buckling events once a critical strain is reached and predicts the propagation of diffusive buckling fronts. The diffusivity and reaction coefficients—and therefore the dynamics—depend on the local lattice geometry, material properties, and strain. Using this, we show how grading the properties of the lattice or introducing defects makes it possible to steer the fronts through the metamaterial, in a targeted and controllable manner.

Experiments

Uniaxial compression tests are performed on 3D-printed, lattice-based metamaterials—consisting of rigid nodes connected by flexible bonds (see Fig. 1A and Materials and methods)—using an universal materials tester (Instron 5600), straining the lattice with a constant crosshead speed of $v = 0.5\,\mathrm{mm\,s^{-1}}$, unless mentioned otherwise. The reaction force F as a function of the applied compression is measured while the structure is observed by a side view camera (Sony alpha 1). All compression tests are repeated four times, rotating the cubic lattice by 90° around the compression axis after the first and third iteration to capture each face's dynamical response twice.

Dynamic response

The dynamical response to uniaxial compression of two slightly different lattice structures is shown as a sequence of images in Fig. 1B. Making the bonds thicker while keeping the node size the same causes the overall response to transition from local buckling (upper row) to global buckling (lower row) once a critical strain, ϵ_{crit}, is reached. During local buckling, the lattice collapses into itself due to counter-rotation of neighboring nodes, which results in an hourglass-like pattern when looked at from the "front" (here the xz-plane). In contrast, during global buckling the middle row shears out to one side and all nodes in the same row co-rotate. With two rotation axes perpendicular to the compression direction, there are four possible rotation directions that can be triggered by the buckling instability, two of which are visible in the images as clockwise and counter-clockwise rotation in the left panels in Fig. 1B, which we define as "front view". The rightmost panels in Fig. 1B show the corresponding "side view," highlighting the difference in self-folding of the five layers as well as the absence of node rotation in the yz-plane. A priori it is unknown which face of the lattice cube will become "front" and "side" during uniaxial compression; however, as long as the time between compression cycles is held short (1 min in our case) the cube "remembers" the state set by the first compression.

To highlight the counter-rotating and co-rotating nature of the nodes during both types of buckling, in Fig. 1C the node rotation angle θ is shown for the center nine nodes of the "front view". Different symbols represent the nodes indicated in the images to the right of each plot. For both cases, we observe that θ starts to bifurcate above a critical strain ϵ_{crit} and—apart from the middle row during global buckling (green triangles)—θ increases with $\epsilon > \epsilon_{\mathrm{crit}}$.

Since the angles bifurcate during buckling, different regions of the lattice might arbitrarily choose a different rotation pattern, which can result in domain walls. Figure 1B shows a deformation pattern that is uniform throughout the lattice when there is sufficiently strong coupling between nodes by relatively thick or stiff bonds. This gives way to nonuniform deformation patterns when the coupling is weak, with domain walls between regions corresponding to differently oriented final states. Figure 1D shows an example for local buckling. When looked at from the front, we see a change in orientation of the pattern at different depths. The side view indicates that the left-most layer has a different rotation pattern compared to the other three, implying that the bonds extending across the domain wall (red region) experience torsion. Given a large enough system, local buckling can generate domain walls also in lattices with a stronger coupling (see Section I).

Global versus local buckling

To map out the conditions under which the response to compression involves global or local buckling, we vary the relative sizes of nodes and bonds as well as the overall lattice size. From Fig. 1E, we find that designs with larger L_{bond} or larger R_{bond} exhibit uniform global buckling (triangles), characterized by shear between successive lattice planes along z and uniform rotation of nodes within each plane. Once L_{bond} or R_{bond} fall below certain threshold values, the deformation pattern switches to local buckling (green diamonds), characterized by alternating bending of the bonds and counter-rotating neighboring nodes within and across layers. For sufficiently thin bonds, we furthermore observe domain wall formation (red squares), whereby the bonds connecting adjacent vertical planes experience twist. As we will show below, in the continuum limit the transition from global buckling (facilitated by shear between lattice planes) to local buckling (facilitated by bond bending) occurs when $4k_b/(k_s L_{\mathrm{bond}}^2) = 1$. Here, the bond bending stiffness $k_b = E_{\mathrm{bond}} I_{\mathrm{bond}}/L_{\mathrm{bond}}$ and the shear stiffness $k_s = \kappa G_{\mathrm{bond}} A_{\mathrm{bond}}/L_{\mathrm{bond}}$ depend on the effective Young's and shear moduli E_{bond} and G_{bond} of the lattice material. Translating this result to a criterion for a lattice fabricated

Downloaded from academic.oup.com/pnasnexus/article/5/8/pgag272/8759452 by guest on 04 November 2026

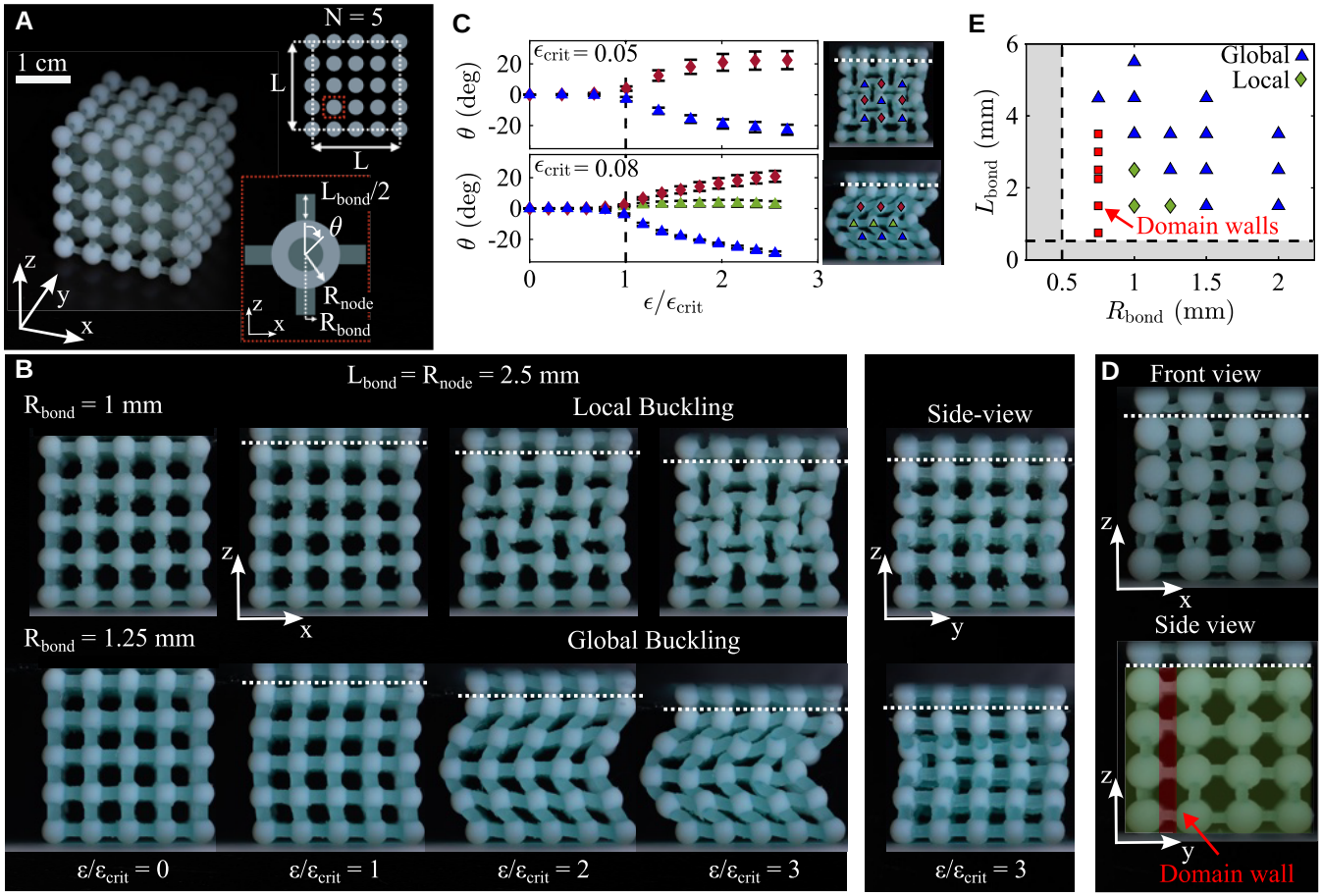


Figure 1 3D-printed cubic lattices under compression. A) 3D-printed cubic lattice with rigid nodes (white) and flexible bonds (light blue) where $N = 5$, $L = 30$mm, $R_{node} = 2.5$mm, $R_{bond} = 0.75$mm, and $L_{bond} = 2.5$mm. B) Sequence of images (front view) showing the dynamical response of two slightly different lattice structures to uniaxial compression, see Movie S1. The overall response transitions from local to global buckling once a critical strain, ϵ_{crit}, is reached. The rightmost panel shows the difference in self-folding of the five layers from the side. The white dotted lines indicate where the bottom of the compression plate touches the top of the lattice. C) Node rotation θ during local and global buckling of the nine center nodes, showing counter-rotating neighbors (upper) and co-rotating rows (lower), respectively. Clockwise rotations are defined positive (see (A)). D) Front- and side view of a compressed cubic lattice with $N = 4$, $R_{node} = 2.63$mm, $R_{bond} = 0.75$mm, and $L = 22.5$mm at $\epsilon = 0.125$, see Movie S2. Within different layers of the cube the orientation of the pattern formation changes (green regions). This leads to torsion of the bonds (red region) connecting these layers and the formation of a domain wall. E) Parameter space in terms of bond length and bond radius indicating the cubic lattices that buckle globally (triangles) or locally (diamonds), including those that show the formation of a domain wall during local buckling (squares).

from rods as bonds and spheres as nodes, we use the bonds' area moment of inertia $I_{bond} = \pi R_{bond}^4/4$ and their cross-sectional area $A_{bond} = \pi R_{bond}^2$. To model the effective stiffness to layer shearing, we use a shear correction factor κ (49) and set $\kappa = \frac{1-\zeta}{\zeta} R_{bond}/L_{bond}$ to capture the decrease of effective shearing stiffness when either the node or the bond radii decrease or when the bond length increases. Here, $\zeta = (N-1)L_{bond}/L$ is the fraction of side length L occupied by bonds. After substituting this for k_b and k_s, the transition criterion becomes

$$\frac{L_{bond}}{R_{bond}} = \frac{E_{bond}}{G_{bond}} \frac{\zeta}{1-\zeta}. \quad (1)$$

According to Eq. 1, the distinct domains that produce global and local buckling can thus be delineated in a plot of bond slenderness, L_{bond}/R_{bond} versus the bond-to-node length ratio, $\zeta/(1-\zeta)$. This is shown in Fig. 2A, which depicts data for the same designs as Fig. 1E. The areas shown in gray fall outside the available design space due to either printer resolution limitations (dashed line) or design restrictions (dotted line). For the lattice structures investigated here, we find the ratio of the effective Young's and shear moduli of the lattice material to be $E_{bond}/G_{bond} = 4$ (red line).

Apart from controlling the type of buckling that will emerge, decreasing the bond radius while keeping the size of the nodes the same allows us to tune the degree to which a lattice can fold into itself under compression. This can be quantified by determining the Poisson's ratio, $\nu = -\epsilon_x/\epsilon_z$, where ϵ_x and ϵ_z are the strain in the transverse and axial direction, respectively. By tracking the positions of the nodes during compression from the "front view", we can determine the instantaneous Poisson's ratio $\nu_{i,k}(\epsilon)$ of every node and take an average of the nine in the center. Figure 2B shows the evolution of this average, $\bar{\nu}$, as a function of strain for four lattices with constant node size but decreasing bond radius. By doing so, we transition from global buckling (dark blue and green diamonds) with $\bar{\nu} > 0$ to local buckling (light blue and red diamonds) with $\bar{\nu} < 0$ beyond a critical strain. Tuning the geometry of the lattice structure thus allows for a broad range of control over the local Poisson's ratio.

Downloaded from academic.oup.com/pnasnexus/article/5/8/pgag272/8759452 by guest on 04 November 2026

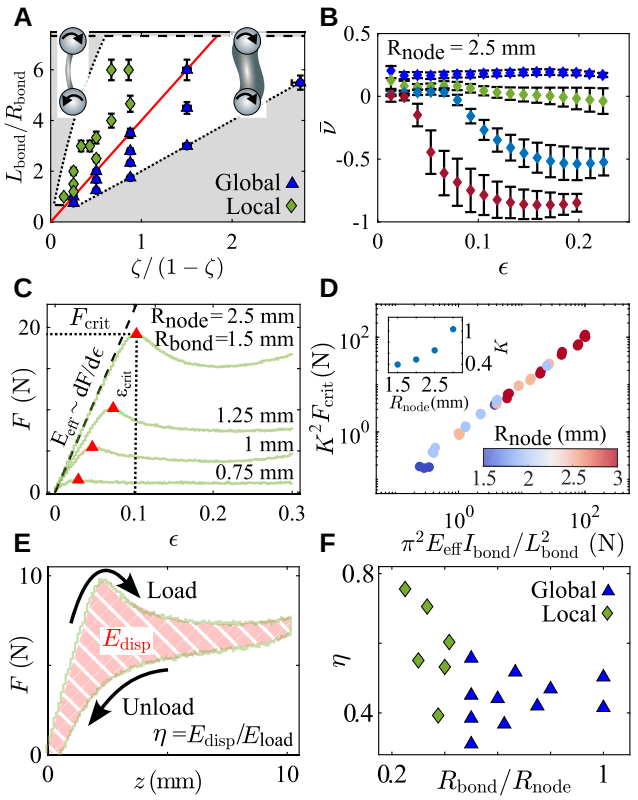


Figure 2 Buckling phase space and mechanical response. A) Parameter space indicating the regions of global (triangles) and local (diamonds) buckling. The gray area is beyond the available design space. The solid red line corresponds to Eq. 1 and its slope is the ratio of the effective Young's and shear moduli of the lattice material $E_{bond}/G_{bond} = 4$. B) Poisson's ratio averaged over the center nine nodes $\bar{\nu}$ as a function of applied strain ϵ for the "front" view. Dark-blue to red, R_{bond} = [2mm, 1.25mm, 1mm, 0.75mm]. C) Reaction force F during compression as a function of strain ϵ for four different lattice designs with $R_{node} = 2.5$mm. The first local maximum indicates F_{crit} and ϵ_{crit} (triangles). The initial slope (dashed line) gives the effective Young's modulus $E_{eff} \sim dF/d\epsilon$ of the lattice. D) Normalized critical buckling force of 15 different designs as a function of material properties on a double-logarithmic scale. Each point represents one experiment and its color reflects the node radius. The inset shows the measured relation between K as a function of R_{node} for these lattices. E) Typical force versus displacement curve to determine the dissipation energy E_{disp} (red shaded area) and the dissipation ratio $\eta = E_{disp}/E_{load}$. F) Dissipation ratio η for different designs with $N = 5$ as a function of R_{bond}/R_{node}. Symbols indicate global (triangles) or local (diamonds) buckling. Standard deviations over three repetitions are within the size of the symbols.

Force response

For four different designs with constant node radius but decreasing bond radius, the force–strain relationships are shown in Fig. 2C. Initially linearly increasing with applied strain, F reaches a maximum before either weakening (negative slope) for thicker bonds or plateauing (zero slope) for thinner ones. The slope of the initial increase relates to the effective Young's modulus of the cubic lattice as $E_{eff} \sim dF/d\epsilon$. Per definition $E_{eff} = d\sigma/d\epsilon$, with σ the local stress. Considering that only the vertical bonds are load-bearing during the initial stages of compression, we write $E_{eff} = (dF/d\epsilon)/(N^2 A_{bond})$.

The reaction force and strain at the first local maximum, F_{crit} and ϵ_{crit}, indicate the critical force and strain at which either global or local buckling occurs. Using the above expression for E_{eff}, the two can be related by $F_{crit} \approx N^2 E_{eff} A_{bond} \epsilon_{crit}$. Based purely on this force–strain relationship, we cannot tell what type of buckling is triggered. Approaching the buckling of the simple cubic lattice as a classical buckling problem of all the load-bearing, vertical bonds, we argue that Euler's critical load criteria should hold (1, 49), which balances bending and compression energies. Hence,

$$F_{crit} = \frac{\pi^2 E_{eff} I_{bond}}{(K L_{bond})^2}, \tag{2}$$

with E_{eff} as defined above, $I_{bond} = \pi R_{bond}^4/4$ the area moment of inertia of the bond, and K a dimensionless prefactor of order unity that effectively changes the lengths of the bond and relates to the applied boundary conditions (49). As we leave the system unconstrained, apart from compression in one direction, the top and bottom boundary nodes are essentially free to rotate and translate in the transverse directions. Since it is unknown how the overall geometry of the lattice will affect the local boundary conditions, and hence the value of K, we measure F_{crit} experimentally and relate this to the known material properties—in line with Eq. 2—to empirically determine this prefactor for different designs. A collapse of the data is achieved and shown on a double-logarithmic scale in Fig. 2D after normalization with K (see inset Fig. 2D). Knowing $K(R_{node})$ for a given set of designs then allows us to predict the critical force (and hence critical strain) at which buckling will occur, given a specific set of lattice material properties.

Energy dissipation

During a loading and unloading cycle, the lattice structures will dissipate a certain amount of energy. To investigate the design-dependent strain energy dissipation, we perform compression cycles for a subset of the designs with $N = 5$ (see Materials and methods) and determine the dissipation ratio $\eta = E_{disp}/E_{load} = 1 - |E_{unload}|/E_{load}$, based on the force-displacement curves, see Fig. 2E. We then quantify for each design the strain energy dissipation in Fig. 2F. We find that designs exhibiting local buckling (diamonds)—and specifically those with thin bonds and large nodes—are more efficient in terms of strain energy dissipation (50) as compared to those structures that exhibit global buckling (triangles).

Our lattice-based metamaterials thus facilitate a platform where node rotation and bond bending during local buckling favor energy dissipation. Being able to nucleate and steer local buckling within such lattice structures in a controllable and predictable manner is the focus of the remainder of this paper.

Continuum model

In order to extend and generalize our experimental observations to larger systems, we aim to construct a mathematical framework allowing us to approach the continuum limit (29–31, 33, 35, 36). Specifically, we wish to describe the temporal evolution of the node rotations within the 3D lattice during compression.

Downloaded from academic.oup.com/pnasnexus/article/5/8/pgag272/8759452 by guest on 04 November 2026

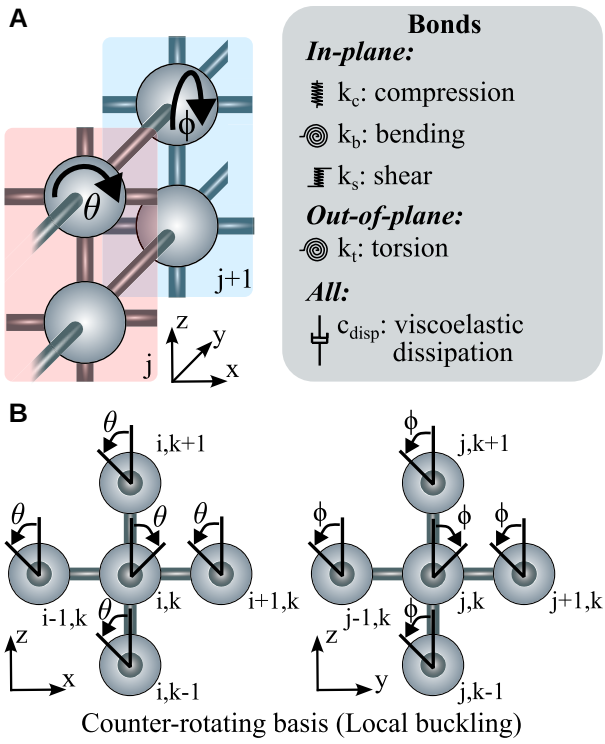


Figure 3 Definitions for 3D-continuum model. A) 3D-schematic indicating different xz-planes (red and blue regions) and the corresponding θ and ϕ node rotations in the xz- and yz-plane, respectively. The box indicates bonds of the cubic lattice that are modeled as axial (compression and shear) or torsional springs (bending and torsion). All bonds experience viscoelastic dissipation. B) Schematic of a sliced portion of the cubic lattice showing the definitions for θ and ϕ in their corresponding planes, as well as the indexing of the nodes. We assume a counter-rotating coordinate transformation within the plane, resembling local buckling.

To this end, we first consider a discrete set of nodes that are connected with flexible bonds. Each node has a rotation angles $\theta_{i,j,k}$ and $\phi_{i,j,k}$ associated within xz- and yz-planes, respectively, and we apply a coordinate transformation in line with the experimental observations on counter-rotating neighbors during local buckling, see Fig. 3. This entails that if $\theta_{i,j,k}/\phi_{i,j,k}$ is defined positive for clockwise rotation, its in-plane neighbors are defined positive for counter-clockwise rotations. We then consider that the connecting bonds act as harmonic springs. For in-plane bonds, we assume axial springs for compression and shear, and torsional springs for bending. For out-of-plane bonds, we assume an additional torsional spring for torsion, connecting nodes of different planes. For all bonds, we lastly assume viscoelastic dissipation, see Fig. 3A. The current model only accounts for node rotations during compression and no translations. The latter are related to the applied axial strain (ϵ_z), as well as ϵ_x and ϵ_y, that relate to the local Poisson's ratio, which is a lattice structure property (see Fig. 2B). Here, we assume that the 3D strains are known and put ourselves in the reference frame of the translating nodes, hence only considering rotation as a degree of freedom. In addition, we impose a constraint on the maximum rotation angle, in line with the experimental observations of nodal contact at sufficiently large strain.

We then have corresponding energies in 1D for bending $(E_b = k_b/2 \sum_k [\theta_k + \theta_{k+1}]^2 + [\phi_k + \phi_{k+1}]^2)$, shearing $(E_s = (L_{\text{bond}}/2)^2 k_s/2 \sum_k [\theta_k - \theta_{k+1}]^2 + [\phi_k - \phi_{k+1}]^2)$, compression $(E_c = -F_z L_{\text{bond}} \sum_k [1 - \cos\theta_k \cos\phi_k])$ and a Rayleigh dissipation function (51, 52) $(\mathcal{F}_\theta(\dot{\theta}) = c_{\text{disp}}/2 \sum_k \dot{\theta}_k^2)$, where k goes from 1 to N and $\dot{\theta} = \partial_t \theta(\vec{x}, t)$ with $\vec{x} = [x, y, z]$. The 3D equivalents of all expressions are listed in the Section II. F_z is the applied force defined positive in the negative z-direction, and $c_{\text{disp}}(\dot{\epsilon})$ is the strain-rate dependent dissipation factor (see Materials and methods). The torsional energy connecting 2D planes is $E_t = k_t/2 \sum_{i,j,k} [\theta_{i,j,k} - \theta_{i,j+1,k}]^2 + [\phi_{i,j,k} - \phi_{i+1,j,k}]^2$, where $k_t = G_{\text{bond}} J_{\text{bond}}/L_{\text{bond}}$, with $J_{\text{bond}} = \pi R_{\text{bond}}^4/2$ the bond's polar moment of intertia. Inertial effects are neglected since we assume to be in the overdamped limit. Its potential effect is discussed in detail in the Section VII, including a dynamical stability analysis and topological defects solutions.

Next, we evaluate a simplified Lagrangian formulation (51) $\partial_{\theta_{i,j,k}}(E_b + E_s + E_c + E_t) + \partial_{\dot{\theta}_{i,j,k}} \mathcal{F}_\theta = 0$ (equivalently for $\phi_{i,j,k}$) and assume expansions for $\theta_{k\pm1} \approx \theta \pm L_{\text{bond}} \partial_z \theta + L_{\text{bond}}^2/2 \partial_z^2 \theta$ (equivalently for θ_{i+1} and θ_{j+1}) to approach the continuum limit. Additionally, we approximate the angles, using $\sin\theta \approx \theta - \theta^3/6$ and $\cos\theta \approx \theta - \theta^2/2$. After evaluation and rearrangement of terms (see Section II for a detailed derivation), we obtain the following set of reaction–diffusion equations:

$$\begin{aligned} \partial_t \theta(\vec{x}, t) &= D_{xz}\left(\partial_x^2 + \partial_z^2\right)\theta(\vec{x}, t) + D_y \partial_y^2 \theta(\vec{x}, t) + f(\theta, \phi), \\ \partial_t \phi(\vec{x}, t) &= D_{yz}\left(\partial_y^2 + \partial_z^2\right)\phi(\vec{x}, t) + D_x \partial_x^2 \phi(\vec{x}, t) + g(\theta, \phi), \end{aligned} \tag{3}$$

with $D_{xz} = D_{yz} = (k_s L_{\text{bond}}^2/4 - k_b) L_{\text{bond}}^2/c_{\text{disp}}$ and $D_y = D_x = k_t L_{\text{bond}}^2/c_{\text{disp}}$ the diffusivity constants in the xz- and yz-planes, and y- and x-directions, respectively. The forcing terms read:

$$\begin{aligned} f(\theta, \phi) &= \mathcal{C}_\theta\left[1 - \tfrac{8k_b}{FL_{\text{bond}}} - \tfrac{\theta(\vec{x}, t)^2}{6} - \tfrac{\phi(\vec{x}, t)^2}{2}\right]\theta(\vec{x}, t), \\ g(\theta, \phi) &= \mathcal{C}_\phi\left[1 - \tfrac{8k_b}{FL_{\text{bond}}} - \tfrac{\phi(\vec{x}, t)^2}{6} - \tfrac{\theta(\vec{x}, t)^2}{2}\right]\phi(\vec{x}, t), \end{aligned} \tag{4}$$

where $\mathcal{C}_\theta = \mathcal{C}_\phi = F_z L_{\text{bond}}/c_{\text{disp}}$. Repeating the derivation in the co-rotating reference frame (resembling global buckling; see Section II) yields a similar set of equations but with $D_{xz}^\star = D_{yz}^\star = (k_b - k_s L_{\text{bond}}^2/4) L_{\text{bond}}^2/c_{\text{disp}}$. The crossover between local and global buckling occurs when the diffusivities associated with these two modes become equal, i.e. when $(k_b - k_s L_{\text{bond}}^2/4) = (k_s L_{\text{bond}}^2/4 - k_b)$, which produces the transition criterion at $4k_b/(k_s L_{\text{bond}}^2) = 1$, that we used earlier in the derivation of Eq. 1.

Static buckling

In the static limit, we can analytically determine the buckling behavior considering $f(\theta, \phi = 0) = 0$, resulting in nontrivial solutions of the form $\theta = \pm(6[1 - 8k_b/(F_z L_{\text{bond}})])^{1/2}$. The solution for θ bifurcates at a critical force—similar to that in Eq. 2 of the whole lattice structure—where now $F_{\text{crit}} = 8k_b/L_{\text{bond}}$. As earlier, $F = N^2 E_{\text{eff}} A_{\text{bond}} \epsilon$ in the initial linear regime (see Materials and methods for a more general alternative), hence $\epsilon_{\text{crit}} = 8k_b/(N^2 E_{\text{eff}} A_{\text{bond}} L_{\text{bond}}) = 8k_b/(N^2 k_c L_{\text{bond}}^2)$. This leads to $\theta = \pm(6[1 - \epsilon_{\text{crit}}/\epsilon])^{1/2}$ with bifurcation occurring at $\epsilon = \epsilon_{\text{crit}}$ and with θ increasing with applied strain—for both local and global buckling—thus in line with the experimental observations in Fig. 1C. Using this, we can rewrite Eq. 4 in terms of strain as

Downloaded from academic.oup.com/pnasnexus/article/5/8/pgag272/8759452 by guest on 04 November 2026

$$f(\theta,\phi)=\mathcal{R}_\theta\epsilon\left[1-\epsilon_{\text{crit}}/\epsilon-\frac{\theta(\vec{x},t)^2}{6}-\frac{\phi(\vec{x},t)^2}{2}\right]\theta(\vec{x},t),$$
$$g(\theta,\phi)=\mathcal{R}_\phi\epsilon\left[1-\epsilon_{\text{crit}}/\epsilon-\frac{\phi(\vec{x},t)^2}{6}-\frac{\theta(\vec{x},t)^2}{2}\right]\phi(\vec{x},t), \quad (5)$$

where $\mathcal{R}_\theta=\mathcal{R}_\phi=N^2k_cL_{\text{bond}}^2/c_{\text{disp}}$. Interestingly, the force terms change sign as we increase the applied strain and transitions from being negative at small strains (sinks) to becoming positive (sources) when $\epsilon\gtrsim\epsilon_{\text{crit}}$. As a consequence, initial perturbations in the node rotations decay prior to buckling but grow during postbuckling.

Buckling plane selection

As a next step, we analyze the stability of the system when both θ and ϕ are nonzero to determine why node rotations and therefore buckling are only observed in one of the planes (see Fig. 1B). We assume a potential energy $V(\theta,\phi)$ for which $\partial V(\theta,\phi)/\partial\theta=-c_{\text{disp}}f(\theta,\phi)=0$ and $\partial V(\theta,\phi)/\partial\phi=-c_{\text{disp}}g(\theta,\phi)=0$ need to be satisfied. If both variables are nonzero they must be equal, leading—after subtraction of the terms in brackets of Eq. 5—to $\theta^2=\phi^2=\xi^2=3(1-\epsilon_{\text{crit}}/\epsilon)/2$. Integration yields a potential energy as

$$V(\theta,\phi)=-c_{\text{disp}}\mathcal{R}\epsilon\left[\left(1-\frac{\epsilon_{\text{crit}}}{\epsilon}\right)\frac{\theta^2+\phi^2}{2}-\frac{\theta^4+\phi^4}{24}-\frac{\theta^2\phi^2}{4}\right], \quad (6)$$

with $\mathcal{R}=\mathcal{R}_\theta=\mathcal{R}_\phi$, resembling the Landau free-energy of a second-order phase transition (53). Determining its Hessian H and substituting $\theta^2=\phi^2=\xi^2$ yields that $\det(H)\propto-2[(1-\epsilon_{\text{crit}}/\epsilon)]^2<0$ (see Section II), which is unstable. However, when $\theta\neq0$ and $\phi=0$ or vice versa, the Hessian is diagonal with positive diagonal elements, representing a stable minimum. This is therefore in line with our experimental observations that only one face of the cubic lattice shows node rotation and pattern formation (front view), whereas rotations are absent on the perpendicular faces (side view), see Fig. 1B.

Numerical evaluation

The evolution of the node rotations can now be determined by numerically evaluating Eqs. 3 and 5 (see Materials and methods). Starting with a randomly perturbed initial state, Fig. 4A shows the temporal evolution of normalized angles $\tilde{\theta}=\theta/\theta_{\text{max}}$ and $\tilde{\phi}=\phi/\phi_{\text{max}}$ within two fixed planes in the counter-rotating basis. Here, $\theta_{\text{max}}=\phi_{\text{max}}=40^\circ$ is the maximum rotation angle of the nodes observed experimentally. As time progresses, the above-mentioned buckling plane selection ensures that $\tilde{\theta}\neq0$ and $\tilde{\phi}=0$ for this case. Next, we can impose an additional initial condition, consistent with our experimental observations, that buckling nucleation sides occur at the least constrained edges of the cubic lattice. We then follow the propagation of the buckling instability through the different layers of the 3D system, leading to the series of snapshots shown in Fig. 4B. Over time a static xz-plane emerges in which the orientation of the local buckling completely changes (from red to blue), indicating the existence of a domain wall (last row Fig. 4B). By varying the strength of the initial perturbation and/or the coupling strength between planes—set by D_x and D_y—the position of this domain wall can shift or can become absent, potentially

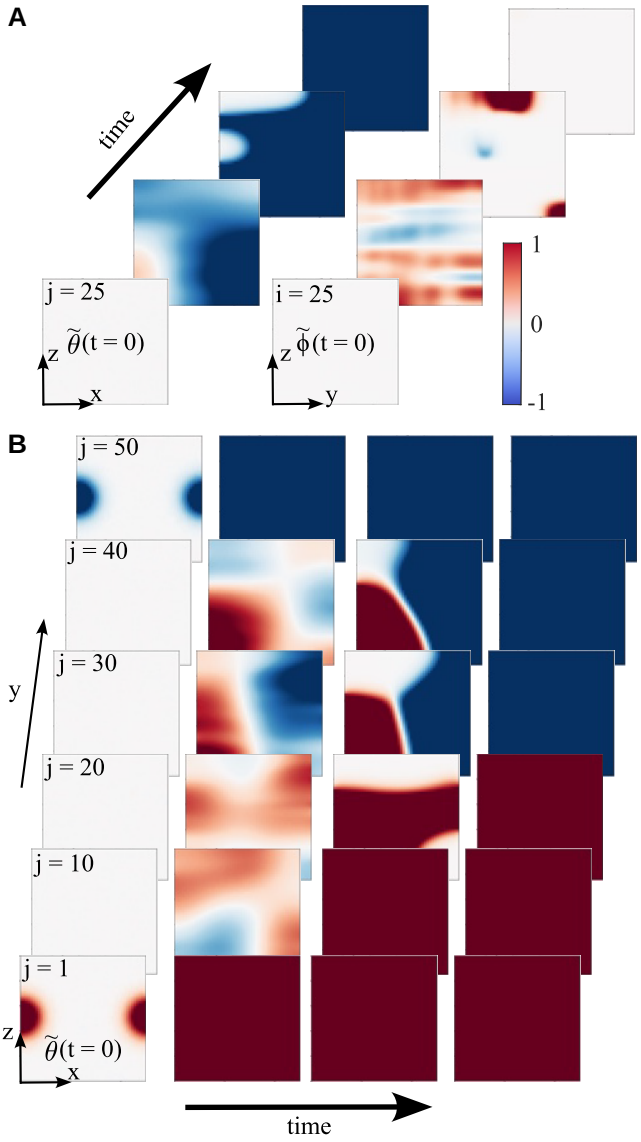


Figure 4 Buckling plane selection and propagation in 3D. A) Cross-sections of the 3D domain showing the temporal evolution of the normalized node rotations $\tilde{\theta}=\theta/\theta_{\text{max}}$ and $\tilde{\phi}=\phi/\phi_{\text{max}}$ in the counter-rotating basis, given random initial angular perturbations. Eventually, a buckling plane is selected with $\tilde{\theta}\neq0$ and $\tilde{\phi}=0$, or vice versa. B) Local buckling propagation through a 3D lattice structure given nucleation sides at the less constrained edges and random initial angular perturbations.

leading to uniform local buckling. Similar behavior is observed in the experiments, see Fig. 1B, E.

Diffusive buckling front propagation

The above analysis indicates that diffusive fronts will propagate within 2D planes of the 3D lattice structure. Especially if the coupling between the different layers is strong (weak) the dynamics within the plane parallel to the compression axis become identical (isolated). To track this propagation, we therefore can use a representative 2D lattice system and, for comparison with the continuum model, scale up the number of nodes to increase resolution. This is shown in Fig. 5A, B for a square lattice with 15×15 nodes (see Materials and methods). We confine the 2D lattice between two acrylic plates spaced 6mm apart to ensure $\phi=0$ (see sketch in

Downloaded from academic.oup.com/pnasnexus/article/5/8/pgag272/8759452 by guest on 04 November 2026

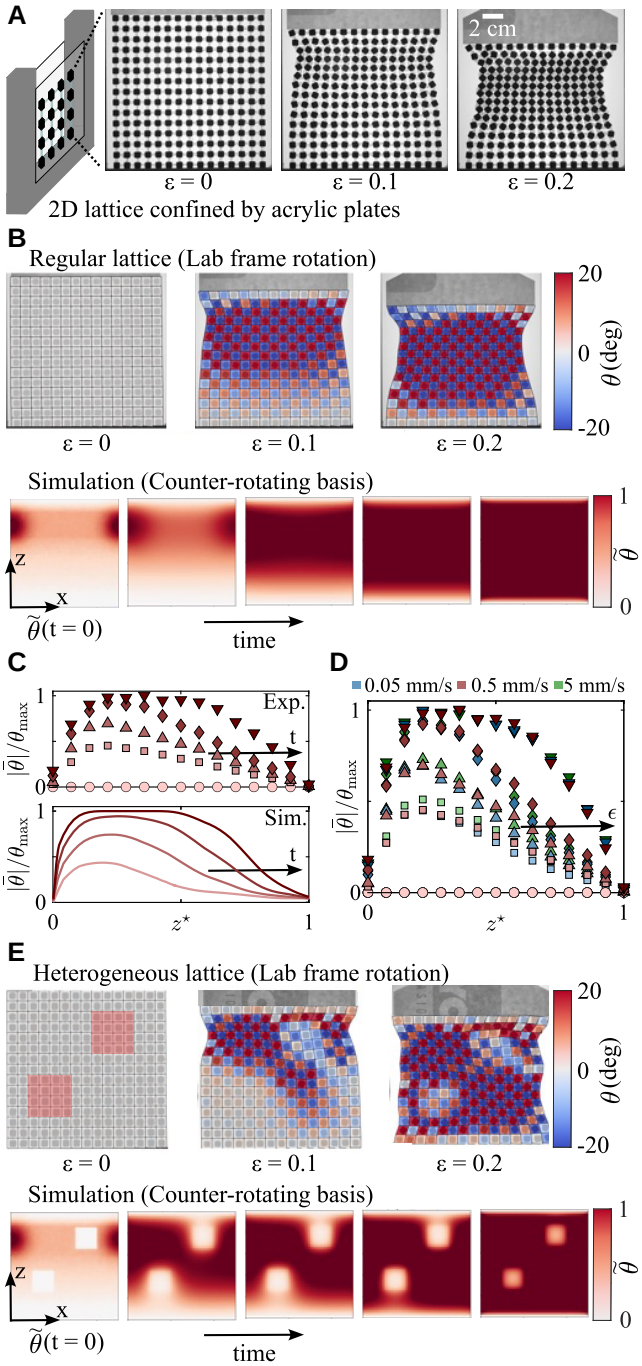


Figure 5 Diffusive buckling fronts in 2D lattices. A) Sketch of setup and sequence of images during compression, see Movies S3 and S4. B) Top: Overlayed node lab frame rotation during compression of the regular lattice. Bottom: 2D simulations with similar initial conditions showing the propagating buckling front in the counter-rotating basis. C) Normalized averages of the rotation angles as a function of rescaled vertical coordinate $z^\star$ at different instances in time, for crosshead speed 0.5 mm s^{-1}. D) Same as C) but for three different crosshead speeds, collapsed by normalizing time by strain rate. Different traces are for different strain. E) Same as B) but with thicker bonds in the indicated regions.

Fig. 5A)—hence biasing the buckling plance selection—and compress the structure, given a target strain and a fixed crosshead speed of $v = 0.5$ mm s^{-1}. A corresponding sequence of images is shown in Fig. 5A. Similar to the 3D cubic lattices, we observe counter-rotation of the nodes, where—due to the confinement—buckling is consistently initiated at the upper edges of the lattice (see Materials and methods). For better indication, we have overlayed the experimental footage with the determined local node rotation in Fig. 5B, highlighting counter-rotation, as well as the formation of a buckling front propagating first inwards and then downwards (see Movie S3). The bottom series of snapshots shows the results after evaluating Eqs. 3 and 5, assuming fixed top and bottom boundaries, and with $\phi = D_y = 0$, as well as initial conditions similar to those in the experiments (see squares in Fig. 5C), showing qualitative agreement.

For better comparison, we take the average of the absolute node rotations at each vertical position, and plot its normalized value as a function of dimensionless and rescaled vertical position $z^\star = 1 - z/(L[1-\epsilon])$, going from top to bottom and taking compression into account, see Fig. 5C. The plots show the evolution of the experimentally observed (top) and numerically simulated (bottom) buckling front with different symbols/colors indicating different instances in time (or strain with $\epsilon = [0.05, 0.1, 0.15, 0.2]$), again showing satisfactory agreement. A quantitive analysis, comparing front location, width and velocity, is in Section V. Given the viscoelastic nature of the polyjet-printed resin (Agilus 30) (54) its material properties are strain-rate dependent. However, over a large range of compression speeds (0.05 mm s^{-1} $\leq v \leq$ 5 mm s^{-1}) the dynamics in our experiments remain unaltered when normalizing time by strain rate (see Fig. 5D and Materials and methods).

Front manipulation

An important outcome of our model is the direct link between lattice design parameters and buckling front propagation. This provides a means for manipulating and steering the fronts. Here, we discuss two examples where this is achieved through local changes in the lattice structure, although changing local material parameters, such as the bond's Young's modulus, provides an alternate approach. In Fig. 5E, bonds within the red regions have been made thicker ($R_{\text{bond}} = 1.5$mm), causing local variations in (i) the diffusivity constant (D_{xz}), (ii) the strength of the source term (R_θ), and (iii) the onset of the latter becoming positive (ϵ_{crit}). This leads to front propagation around these regions—as predicted by the dynamic buckling model by assuming different coefficients locally—followed by their delayed buckling onset. Steering is also achieved by generating structural defects, such as randomly misplaced bonds, within suitably identified regions, which retards node rotation and causes the formation of (temporary) internal boundaries (see Movies S3 and S4). The same methodology might now be applied to 3D-networks allowing for an expanded design space to enhance instability propagation, shielding of certain regions, or potentially (local) force attenuation—all of which are future research directions still to be explored. The latter might be of particular interest as we find that the amount of energy dissipated during one loading cycle is strongly dependent on lattice structure (see Materials and methods and Section III).

Conclusions

Investigating the dynamic buckling behavior under uniaxial compression of 3D-printed, regular lattice-based metamaterials

Downloaded from academic.oup.com/pnasnexus/article/5/8/pgag272/8759452 by guest on 04 November 2026

comprised of flexible bonds connecting rigid nodes, we mapped the design space that controls different buckling modes, delineating the transition from global to local buckling. In these dissipative, overdamped structures we find that local buckling, triggered by exceeding a threshold strain, propagates as diffusive front. Increasing the bond slenderness changes the response to applied strain from uniform local buckling patterns to non-uniformly buckled configurations, where weak coupling accommodates domain walls between regions corresponding to differently oriented configurations. Bond slenderness also controls the strain-dependent Poisson's ratio, making it possible to move from normal elastic to deeply auxetic behavior.

A 3D-continuum model for the evolution of the node rotations during buckling in overdamped, lattice-based metamaterials leads to a set of coupled reaction–diffusion equations. Both forcing terms change sign with increasing applied strain, transitioning from being sinks to source terms that enhance node rotation. The model, validated by our experiments, captures the onset and the propagation of buckling instabilities through coefficients that depend on material properties as well as local geometry. We show that this opens up opportunities for deliberate manipulation and control of cascading buckling events, for example by designing heterogeneities into the lattice. Since local bond bending and node rotation are essential for the formation of diffusive buckling front that allow for controlled manipulation, lattice designs should not be too restrictive for node rotations. We expect that this approach could be reversed and used to extract the local material properties in a given metamaterial, in particular when combined with physics-based machine learning (55). While our experiments and modeling apply to the regime where material properties can be taken as constant, the viscoelastic behavior of polyjet-printed resin should, in principle, also make it possible to enter regimes where the dynamical response of the metamaterial becomes trainable (56). In that case, repeated forcing via an appropriately chosen training protocol could condition the structures to respond in a targeted manner (57, 58).

Materials and methods

Experiments

The lattice-based metamaterials are fabricated using a high-resolution polyjet 3D-printer capable of multimaterial deposition (Stratasys J850). The structures are lattices with rigid nodes (VeroWhite Polyjet Resin) connected by flexible bonds (Agilus 30 Polyjet Resin, Shore-A40), see Fig. 1A. Although the mechanical response is dependent on the loading-rate, the most important feature for our study, namely the dynamics of the node rotations, remain unchanged upon proper normalization for compressions up to $v_{\text{crosshead}} = 50\,\text{mm}\,\text{s}^{-1}$ (see Section IV). For the 3D simple cubic lattice, we restrict ourselves to $N = \{4, 5\}$ number of nodes per side (hence 64 or 125 nodes in total), inner lattice size $18\text{mm} \leq L \leq 33.75\text{mm}$, node radius $1\text{mm} \leq R_{\text{node}} \leq 3.35\text{mm}$ and bond radius $0.75\text{mm} \leq R_{\text{bond}} \leq 2\text{mm}$ (see Fig. 1A). The bond length is set by the geometrical relation $L_{\text{bond}} = [L - (2N-2)R_{\text{node}}]/[N-1]$ and the printer resolution is $\pm 50\mu\text{m}$. Imperfections during printing with respect to bond thickness and stiffness might bias the location of the domain wall, yet the buckling plane selection is found to be robust against local and small imperfections caused during 3D printing.

For the loading and unloading experiments we compress the structure to a target strain of $\epsilon = 0.3$ with crosshead speed $v = 0.5\,\text{mm}\,\text{s}^{-1}$, pause for 5s, and unload at the same velocity. The mechanical work associated with the force-displacement cycle is calculated by integrating the force over displacement, $E = \int_\delta F(z)\,dz$ where δ denotes the relevant loading or unloading path. By construction, $E_{\text{load}} > 0$ and $E_{\text{unload}} < 0$. The dissipated energy, corresponding to the area enclosed by the force-displacement loop, is then $E_{\text{disp}} = E_{\text{load}} - |E_{\text{unload}}|$. Further details are provided in Section III.

For the 2D experiments, we consider a 15×15 lattice where the spherical nodes are replaced by squares with side lengths of 6mm and the bonds have radius $R_{\text{bond}} = 1\text{mm}$. The length of the entire lattice is $L = 14\text{cm}$. Compressions are recorded using a camera (Sony alpha 1) and back-lighting. Due to confinement by the acrylic plates in the 2D setup (see Fig. 5A), we observe that buckling is consistently initiated at the upper edges of the lattice. The reason for this is the friction between the nodes and the acrylic plates, which introduces a slight gradient in the strain field along the z-direction. Since $\theta(\vec{x}, t) = \pm(6[1 - \epsilon_{\text{crit}}/\epsilon(\vec{x}, t)])^{1/2}$, the nodes in the upper rows reach the critical strain first and start to buckle. Additional design configurations are discussed in Section VI.

Transition between force- to strain-driven buckling

In the derivation of the continuum model, we assumed a linear relation between the applied force and the experienced strain, through $F = N^2 E_{\text{eff}} A_{\text{bond}} \epsilon$, as a simplified approach to transition from a force- to a strain-driven system. More generally, any functional relation where $F = h(\epsilon)$ can be substituted in Eq. 4 to more closely approximate the experiments (see Fig. 2C).

Numerical evaluation

We numerically evaluate the dimensionless versions of Eqs. 3 and 5 through a first-order finite difference method with Neumann boundary conditions at the sides and fixed boundaries at top and bottom, in a domain with dimensions $L_x = L_y = L_z = 50$ (see Section IV). For modeling our strain-driven experiments, we set $\epsilon = \epsilon_0 + \dot{\epsilon}t$ with an initial value for ϵ_0 that can be lower or equal to ϵ_{crit}, where typically $\epsilon_{\text{crit}} = 0.05$. The strain rate is chosen to match experiments, with $\dot{\epsilon} = 3 \times 10^{-3}$ as typical value. Through matching of the profiles in Fig. 5C, we find $D_{xz}/L_{\text{bond}}^2 = \mathcal{O}(1)$ and $\mathcal{R} = \mathcal{O}(1)$ (see Section IV).

Strain-rate dependence

The dissipation factor $c_{\text{disp}}(\dot{\epsilon})$ is a function of strain rate $\dot{\epsilon}$. In particular, $c_{\text{disp}}(\dot{\epsilon}) = \eta_{\text{eff}}(\dot{\epsilon}) V_{\text{bond}}$ (51, 59), with $\eta_{\text{eff}}(\dot{\epsilon})$ the effective viscosity of the system. For viscoelastic materials experiencing oscillatory strain $\eta_{\text{eff}} = E''(\omega)/\omega$ (59), where ω is the oscillation frequency and $E''(\omega)$ the frequency dependent loss modulus. Hence, it is reasonable to assume that in our case $\eta_{\text{eff}} \propto E''(\dot{\epsilon})/\dot{\epsilon}$. To test whether changes in loss modulus E'' are significantly affecting the dynamics when we vary the strain rate, we performed additional experiments

Downloaded from academic.oup.com/pnasnexus/article/5/8/pgag272/8759452 by guest on 04 November 2026

on the 2D lattice at $v = [0.05\,\mathrm{mm\,s^{-1}}, 5\,\mathrm{mm\,s^{-1}}]$, i.e. an order of magnitude smaller and larger than for the data in Fig. 5C. At identical instances of strain, obtained by normalizing time with the corresponding strain rates, we observe a collapse of the experimental data, see Fig. 5D, where curves start to deviate slightly only at high strain rates and at initial times below the critical point. Over the range tested in our experiments we can therefore take E'' as approximately constant and $c_{\mathrm{disp}}(\dot{\epsilon}) \propto E'' V_{\mathrm{bond}}/\dot{\epsilon}$. This means that decreasing the strain rate $\dot{\epsilon}$ simply increases the effective viscosity η_{eff} and slows down the dynamics of the system, while our continuum model remains valid. When the strain rate exceeds the range tested here the loss modulus might change. In addition, material properties like the bond's Young's and shear moduli, as well as the onset of buckling might vary at higher strain rates, and eventually inertial effects would need be considered. A discussion is provided in Sections IV and VII.

Supplementary material

Supplementary material is available at *PNAS Nexus* online.

Competing interest

The authors declare no competing interests.

Funding

This work was supported by the Army Research Office under award W911NF-24-2-0184. The University of Chicago Materials Research Science and Engineering Center, which is supported by the National Science Foundation under award DMR-2011854, provided additional support for sample fabrication through its shared experimental facilities and for F.S. through its Research Experience for Undergraduates summer program.

Author contributions

Jochem G. Meijer (Conceptualization, Data curation, Formal analysis, Validation, Investigation, Visualization, Methodology, Writing—original draft), Faadil H. Shaik (Formal analysis, Validation, Visualization, Writing—original draft), Victoria V. McDermott (Data curation, Formal analysis, Investigation), and Heinrich M. Jaeger (Conceptualization, Supervision, Funding acquisition, Methodology, Writing—original draft, Project administration).

Data availability

The materials underlying this study are provided in the Supplementary Material. Additional data and details supporting the findings are available in the Materials Data Facility public repository (DOI: https://doi.org/10.18126/089t-7503).

References

1. Euler L. *Methodus inveniendi lineas curvas maximi minimive proprietate gaudentes sive solutio problematis isoperimetrici latissimo sensu accepti*. Vol. 1. Springer Science & Business Media, 1952. (orignal 1744).
2. Bertoldi K, Vitelli V, Christensen J, Van Hecke M. 2017. Flexible mechanical metamaterials. *Nat Rev Mater*. 2:1–11.
3. Mullin T, Deschanel S, Bertoldi K, Boyce MC. 2007. Pattern transformation triggered by deformation. *Phys Rev Lett*. 99: 084301.
4. Bertoldi K, Boyce MC, Deschanel S, Prange SM, Mullin T. 2008. Mechanics of deformation-triggered pattern transformations and superelastic behavior in periodic elastomeric structures. *J Mech Phys Solids*. 56:2642–2668.
5. Lakes R. 1987. Foam structures with a negative Poisson's ratio. *Science*. 235:1038–1040.
6. Grima JN, Evans KE. 2000. Auxetic behavior from rotating squares. *J Mater Sci Lett*. 19:1563–1565.
7. Grima JN, Alderson A, Evans KE. 2005. Auxetic behaviour from rotating rigid units. *Phys Status Solidi (b)*. 242:561–575.
8. Gaspar N, Ren XJ, Smith CW, Grima JN, Evans KE. 2005. Novel honeycombs with auxetic behaviour. *Acta Mater*. 53: 2439–2445.
9. Wang G, Al-Ostaz A, Cheng AH-D, Mantena PR. 2009. Hybrid lattice particle modeling: theoretical considerations for a 2d elastic spring network for dynamic fracture simulations. *Comput Mater Sci*. 44:1126–1134.
10. Bertoldi K, Reis PM, Willshaw S, Mullin T. 2010. Negative Poisson's ratio behavior induced by an elastic instability. *Adv Mater*. 22:361–366.
11. Greaves GN, Greer ALindsay, Lakes RS, Rouxel T. 2011. Poisson's ratio and modern materials. *Nat Mater*. 10:823–837.
12. Nicolaou ZG, Motter AE. 2012. Mechanical metamaterials with negative compressibility transitions. *Nat Mater*. 11: 608–613.
13. Reid DR, *et al.* 2018. Auxetic metamaterials from disordered networks. *Proc Natl Acad Sci U S A*. 115:E1384–E1390.
14. Overvelde JTB, Shan S, Bertoldi K. 2012. Compaction through buckling in 2d periodic, soft and porous structures: effect of pore shape. *Adv Mater*. 24:2337–2342.
15. Mullin T, Willshaw S, Box F. 2013. Pattern switching in soft cellular solids under compression. *Soft Matter*. 9:4951–4955.
16. Overvelde JohannesTB, Bertoldi K. 2014. Relating pore shape to the non-linear response of periodic elastomeric structures. *J Mech Phys Solids*. 64:351–366.
17. Cho Y, *et al.* 2014. Engineering the shape and structure of materials by fractal cut. *Proc Natl Acad Sci U S A*. 111: 17390–17395.
18. Shan S, Kang SH, Zhao Z, Fang L, Bertoldi K. 2015. Design of planar isotropic negative Poisson's ratio structures. *Extreme Mech Lett*. 4:96–102.
19. He Y, Zhou Y, Liu Z, Liew KM. 2018. Buckling and pattern transformation of modified periodic lattice structures. *Extreme Mech Lett*. 22:112–121.
20. Cutolo A, Palumbo S, Carotenuto AR, Sacco E, Fraldi M. 2022. A class of periodic lattices for tuning elastic instabilities. *Extreme Mech Lett*. 55:101839.
21. Dykstra DavidMJ, Janbaz S, Coulais C. 2022. The extreme mechanics of viscoelastic metamaterials. *APL Mater*. 10:080702–080702–11.
22. Coulais C, Overvelde JohannesTB, Lubbers LA, Bertoldi K, van Hecke M. 2015. Discontinuous buckling of wide beams and metabeams. *Phys Rev Lett*. 115:044301.

Downloaded from academic.oup.com/pnasnexus/article/5/8/pgag272/8759452 by guest on 04 November 2026

23. Nadkarni N, Arrieta AF, Chong C, Kochmann DM, Daraio C. 2016. Unidirectional transition waves in bistable lattices. *Phys Rev Lett*. 116:244501.
24. Raney JR, *et al.* 2016. Stable propagation of mechanical signals in soft media using stored elastic energy. *Proc Natl Acad Sci U S A*. 113:9722–9727.
25. Jin L, *et al.* 2020. Guided transition waves in multistable mechanical metamaterials. *Proc Natl Acad Sci U S A*. 117: 2319–2325.
26. Yasuda H, Korpas LM, Raney JR. 2020. Transition waves and formation of domain walls in multistable mechanical metamaterials. *Phys Rev Appl*. 13:054067.
27. Librandi G, Tubaldi E, Bertoldi K. 2021. Programming nonreciprocity and reversibility in multistable mechanical metamaterials. *Nat Commun*. 12:3454.
28. Nadkarni N, Daraio C, Kochmann DM. 2014. Dynamics of periodic mechanical structures containing bistable elastic elements: from elastic to solitary wave propagation. *Phys Rev E*. 90:023204.
29. Deng B, Raney JR, Tournat V, Bertoldi K. 2017. Elastic vector solitons in soft architected materials. *Phys Rev Lett*. 118: 204102.
30. Deng B, Wang P, He Q, Tournat V, Bertoldi K. 2018. Metamaterials with amplitude gaps for elastic solitons. *Nat Commun*. 9:3410.
31. Mo C, Singh J, Raney JR, Purohit PK. 2019. Cnoidal wave propagation in an elastic metamaterial. *Phys Rev E*. 100: 013001.
32. Gomez M, Moulton DE, Vella D. 2019. Dynamics of viscoelastic snap-through. *J Mech Phys Solids*. 124:781–813.
33. Deng B, Li J, Tournat V, Purohit PK, Bertoldi K. 2021. Dynamics of mechanical metamaterials: a framework to connect phonons, nonlinear periodic waves and solitons. *J Mech Phys Solids*. 147:104233.
34. Deng B, Raney JR, Bertoldi K, Tournat V. 2021. Nonlinear waves in flexible mechanical metamaterials. *J Appl Phys*. 130:040901
35. Veenstra J, *et al.* 2024. Non-reciprocal topological solitons in active metamaterials. *Nature*. 627:528–533.
36. Deng B, Yu S, Forte AE, Tournat V, Bertoldi K. 2020. Characterization, stability, and application of domain walls in flexible mechanical metamaterials. *Proc Natl Acad Sci U S A*. 117:31002–31009.
37. Nachbar W, Huang NC. 1967. Dynamic snap-through of a simple viscoelastic truss. *Q Appl Math*. 25:65–82.
38. Santer M. 2010. Self-actuated snap back of viscoelastic pulsing structures. *Int J Solids Struct*. 47:3263–3271.
39. Stern M, Jayaram V, Murugan A. 2018. Shaping the topology of folding pathways in mechanical systems. *Nat Commun*. 9:4303.
40. Janbaz S, McGuinness M, Zadpoor AA. 2018. Multimaterial control of instability in soft mechanical metamaterials. *Phys Rev Appl*. 9:064013.
41. Janbaz S, Narooei K, Van Manen T, Zadpoor AA. 2020. Strain rate–dependent mechanical metamaterials. *Sci Adv*. 6: eaba0616.
42. Bossart A, Dykstra DavidMJ, Van der Laan J, Coulais C. 2021. Oligomodal metamaterials with multifunctional mechanics. *Proc Natl Acad Sci U S A*. 118:e2018610118.
43. Nadkarni N, Daraio C, Abeyaratne R, Kochmann DM. 2016. Universal energy transport law for dissipative and diffusive phase transitions. *Phys Rev B*. 93:104109.
44. Janbaz S, Coulais C. 2024. Diffusive kinks turn kirigami into machines. *Nat Commun*. 15:1255.
45. Murray JD. 1981. A pre-pattern formation mechanism for animal coat markings. *J Theor Biol*. 88:161–199.
46. Kondo S, Miura T. 2010. Reaction-diffusion model as a framework for understanding biological pattern formation. *Science*. 329:1616–1620.
47. Lacalli TC. 2022. Patterning, from conifers to consciousness: Turing's theory and order from fluctuations. *Front Cell Dev Biol*. 10:871950.
48. McDougal RA, Hines ML, Lytton WW. 2013. Reaction-diffusion in the neuron simulator. *Front Neuroinform*. 7:28.
49. Timoshenko SP, Gere JM. *Theory of elastic stability*. Courier Corporation, 2012.
50. Yin L, Zhang M, Zhu Y, Li B, Wen Y. 2024. Quasi-static cyclic tension–compression behavior of circular anti-chiral auxetic metamaterials. *Constr Build Mater*. 450:138519.
51. Landau LD, Pitaevskii LP, Kosevich AM, Lifshitz EM. *Mechanics*. Vol. 1. Cambridge University Press, 1960.
52. Ginsberg JH. *Advanced engineering dynamics*. Cambridge University Press, 1998.
53. Chaikin PM, Lubensky TC, Witten TA. *Principles of condensed matter physics*. Vol. 10. Cambridge University Press, 1995.
54. Abayazid FF, Ghajari M. 2020. Material characterisation of additively manufactured elastomers at different strain rates and build orientations. *Addit Manuf*. 33:101160.
55. Hernández Q, Win M, O'Connor TC, Arratia PE, Trask N. 2025. Data-driven particle dynamics: structure-preserving coarse-graining for emergent behavior in non-equilibrium systems. *Proc Natl Acad Sci U S A*. 123:e2519631123.
56. Jaeger HM, Murugan A, Nagel SR. 2024. Training physical matter to matter. *Soft Matter*. 20:6695–6701.
57. Gowen SD, *et al.* 2025. Training and retraining liquid crystal elastomer metamaterials for pluripotent functionality. *Proc Natl Acad Sci U S A*. 122:e2504304122.
58. Gowen SD. 2025. Training allostery-inspired mechanical response in disordered elastic networks. *Soft Matter*. 21: 3527–3533.
59. Landau LD, Pitaevskii LP, Kosevich AM, Lifshitz EM. *Theory of elasticity: volume 7*. Elsevier, 2012.

Downloaded from academic.oup.com/pnasnexus/article/5/8/pgag272/8759452 by guest on 04 November 2026